



1 Impact of boundary layer stability on urban park
2 cooling effect intensity

3

4 *Authors: Martial Haeffelin¹, Jean-François Ribaud², Jonnathan Céspedes², Jean-*
5 *Charles Dupont³, Aude Lemonsu⁴, Valéry Masson⁴, Tim Nagel⁴, Simone Kotthaus²*

6

7 ¹ *Institut Pierre Simon Laplace (IPSL), CNRS, Ecole polytechnique, Institut Polytechnique de Paris, 91128*

8 *Palaiseau Cedex, France*

9 ² *Laboratoire de Météorologie Dynamique (LMD-IPSL), Ecole polytechnique, Institut Polytechnique de*

10 *Paris, 91128 Palaiseau Cedex, France*

11 ³ *Institut Pierre Simon Laplace (IPSL), Université Versailles Saint-Quentin-en-Yvelines, 78240*

12 *Guyancourt, France*

13 ⁴ *Centre national de recherches météorologiques (CNRM), Université de Toulouse, Météo-France,*

14 *CNRS, Toulouse, France*

15

16 Correspondence to: Martial Haeffelin (martial.haeffelin@ipsl.fr)



17 Abstract

18 The added heat in cities amplifies the health risks of heat waves. At night under calm winds
19 and cloud free skies, the air in the urban canopy layer can be several degrees warmer than in
20 rural areas. This lower nocturnal cooling in the built-up settings poses severe health risks to
21 the urban inhabitants as indoor spaces cannot be ventilated effectively. With heat waves
22 becoming more frequent and more intense in future climates, many cities are expanding their
23 green spaces with the aim to introduce cooling through shading, evaporation, and lower heat
24 storage capacities. In this study, it is assessed how the evening and night-time cooling effect
25 of urban parks (relative to near-by built-up settings) varies with the park size and the meso-
26 scale atmospheric conditions during warm summer periods. Using a combination of
27 meteorological surface station data and compact radiosondes, the cooling effect is quantified
28 for several urban parks (about 15 ha) and urban woods (about 900 ha). A profiling Doppler
29 wind lidar deployed in the city centre is used to measure turbulent vertical mixing conditions
30 in the urban boundary layer. We find that the maximum nocturnal cooling effects in urban
31 parks range around 1-5°C during a one-week heat wave event in mid-July 2022 but also in
32 general during summer 2022 (June-August). Three atmospheric stability and mixing regimes
33 are identified that explain the night-to-night variability in park cooling effect. We find that
34 very low turbulent vertical mixing in the urban boundary layer ($< 0.05 \text{ m}^2\text{s}^{-2}$) results in the
35 strongest evening cooling in both rural settings and urban parks and the weakest cooling in
36 the built-up environment. This regime specifically occurs during heat waves in connection
37 with large-scale advection of hot air over the region and corresponding subsidence. When
38 nocturnal turbulent vertical mixing above the city is stronger, the evening cooling in urban
39 green spaces is less efficient so that the atmospheric stratification above both urban parks
40 and woods is less stable and temperature contrasts compared to the built-up environment
41 are less pronounced. These results highlight that urban green spaces have a significant cooling
42 potential during heat waves, with maximum effects at night as advection and mixing transport
43 processes are minimal. This suggests adapting the opening hours of public parks to enable
44 residents to benefit from these cooling islands.

45



46 1 - Introduction

47 Excess heat in cities has impacts on human comfort, labour productivity, and health. Mortality
48 has been linked to exceptionally high temperatures during summertime heat waves both at
49 night and during the day (Basu et al. 2002; Keatinge et al. 2000; Pirard et al. 2005). During the
50 day, it is the outdoor radiative temperature that poses the most significant health risk. At
51 night, indoor temperatures are particularly important as people need to rest and indoor air
52 must be vented to cool the building for the upcoming day. However, urban inhabitants can
53 be particularly exposed to excessive and prolonged heat stress at night as the city and the
54 buildings do not cool efficiently, preventing necessary nocturnal rest. Hot nights following hot
55 days have been shown to make an important contribution to heat-related mortality (Murage
56 et al. 2017; Royé et al., 2021).

57

58 Reducing people's exposure to heat in cities can be addressed through urban planning
59 strategies. Increasing the vegetation fraction of urban areas is a widely accepted strategy to
60 mitigate urban heat risk by effectively reducing heat storage uptake during daytime
61 (Grimmond and Oke, 2002). Trees can provide efficient shading whereby reducing daytime
62 air temperatures by several degrees below their canopy, while evapotranspirative cooling
63 provided by vegetation, including trees, shrubs and grass, maintain the green space
64 temperature several degrees below that of the built-up environment (Shashua-Bar and
65 Hoffman, 2000). The green infrastructures also show cooling effects at night, through
66 continued evapotranspiration after sunset, generally larger sky-view factors in urban parks
67 than in built-up environments, and lower heat capacities. However, reduced radiative cooling
68 and ventilation can retain heat below the canopy at night (Taha et al. 1991).

69

70 The cooling effect intensity of urban green infrastructure has been shown to be highly variable
71 (Bowler et al. 2010; Shoulika et al 2014). Doick et al (2014) point to a lack of certainty on the
72 variables that drive the park cooling effects and on the multiple roles of trees and
73 greenspaces. Spatial contrasts in nocturnal temperatures between green infrastructure and
74 nearby built-up areas depend on park perimeter and area (Gao et al. 2022; Cai et al. 2023),
75 on proportion of grass and trees, on tree size (Zhu et al. 2021), on vegetation types and
76 arrangements (street trees vs parks), on density of vegetation (Holmer et al 2013), on park



77 topography (Barradas 1991; Chang et al. 2007), and on local climates (Ibsen et al. 2021). Other
78 authors investigated the spatial extent of cooling by urban parks, i.e. the *cooling effect*
79 *distance*, showing that it depends on both park size and park greenness (e.g. Zhu et al. 2021).
80 From a recent review of park cooling effect studies conducted by Aram et al. (2019), we
81 conclude that most studies focus on the impact of park characteristics and investigations on
82 the impact of meteorological conditions on park cooling effects are rare.

83

84 The impact of meteorological conditions, such as cloudiness, wind and turbulence on
85 differential cooling is studied mostly at regional scale in terms of their impact on the urban
86 heat island (UHI) intensity (Oke 2017). While the influence of cloud cover and wind is rather
87 established (e.g. Morris et al. 2001, Lin et al. 2022), also the occurrence and characteristics of
88 night-time low-level jets are found to influence UHI intensity (Lemonsu et al. 2009; Cespedes
89 et al. 2024). However, the impact of local- to meso-scale meteorological phenomena on
90 cooling effects of urban green infrastructure is not well quantified.

91

92 The combined effects of green infrastructure characteristics and meteorological regimes on
93 nocturnal cooling must hence be better understood so that the cooling effect of urban
94 renaturation projects can be quantified more precisely. Which conditions affect the park
95 cooling effect intensity? What is the relative impact of park characteristics and meteorological
96 processes in the urban boundary layer on the cooling intensity ?

97

98 The overall objective of this study is to quantify in detail the nocturnal cooling effects of urban
99 parks during warm summertime conditions, taking into account potential cooling effects from
100 the rural surroundings. We carried out this study in the framework of the Heat and Health in
101 Cities project (H2C, Lemonsu et al. 2024) that focuses on the effects of excessive summertime
102 heat and air pollution on human vulnerability (Forceville et al. 2024) with the Paris region
103 (France) as a study area. A dedicated field campaign was designed and carried out in the city
104 of Paris and the surrounding region to monitor spatial and temporal variations in key
105 atmospheric thermodynamic variables in the urban canopy layer and urban boundary layer
106 during summer 2022. The measurements performed, including near-surface and vertical
107 profiles of temperature, humidity, wind and turbulence, and data analysis methodology are
108 presented in Section 2. Section 3 presents the analysis of urban park cooling effects in relation



109 to regional UHI and their variability during summer 2022, with a focus on a one-week heat
110 wave event. Next (Section 4), we investigate the characteristics of the urban boundary layer
111 structure under three distinct atmospheric turbulence regimes and their influence on park
112 cooling effects. Finally, we quantify the role of atmospheric stability and vertical turbulent
113 mixing on differential evening cooling between built-up locations, urban parks and rural
114 settings (Section 5).

115

116 2 - Data and methodologies

117 The present study is based upon data collected in the Paris region during the first Special
118 Observation Period of the Heat and Health in Cities project (SOP 2022, Figure 1), which was
119 conducted during summer 2022 (Lemonsu et al., 2024ab). This campaign also benefited from
120 measurements carried out in the context of other research initiatives such as the Paris 2024
121 Olympics WMO Research and Development Project (RDP-2024) and the ACTRIS research
122 infrastructure (Laj et al. 2024). This multi-project context motivated the pooling of resources,
123 a coordinated strategy for the organisation of the summer-2022 experimental campaigns, and
124 the development of a joint data repository under the name PANAME (PARis region urbaN
125 Atmospheric observations and models for Multidisciplinary rEsearch - see
126 <https://paname.aeris-data.fr/>).

127

128 2.1 Datasets used in the study

129 This study combines continuous measurements collected from June to August 2022 and 14
130 one-day intensive observation periods (IOPs), with data collected from mid-June to the end
131 of July 2022. Measurement locations are shown in Figure 1.

132

133 i) Surface meteorological stations

134 Météo France's operational network consists of some fifty ground-based weather stations in
135 the Paris region measuring at least air temperature at 2 m AGL with a 6-minute acquisition
136 time step. A few stations provide additional meteorological parameters such as wind speed
137 and direction at 10 m AGL, global incoming radiation, precipitation, and cloud cover. The



138 stations are spread across the region in different areas, but are always installed on the ground
139 on an open lawn (according to WMO recommendations).

140

141 We selected six stations to represent rural settings (Local Climate Zone, Stewart and Oke
142 2012) of the Paris region (Figure 1), located in Changis, Courdimanche, Fresnoy-La-Riviere,
143 Maule, Melun, and Pontoise, which is similar to the stations selected by Lemonsu et al. (2015).
144 The stations are geographically distributed in all directions relative to the city centre of Paris
145 and located at altitudes ranging 50-90 m above sea level (ASL). In our study, the reference
146 rural setting conditions of temperature, wind speed and direction are computed as the
147 average of the variables measured at those six stations (Changis, Courdimanche, Melun, and
148 Pontoise stations).

149

150 Near-surface urban park weather conditions are documented by a Météo-France weather
151 station located in the Montsouris Park, a 15-ha park located in the 14th district, south of the
152 Paris city centre. The station, located at an elevation of 75 m ASL, provides 2-m air
153 temperature and humidity measurements. Wind speed and direction are measured at 25 m
154 above ground level (AGL). A detailed description of temperature measurements in the
155 Montsouris Park is provided by Dahech et al. (2020).

156

157 The Paris built-up setting conditions are sampled using Internet of Things (IoT) temperature
158 and humidity measurements. This compact technology opens up new perspectives in
159 meteorological measurements, particularly in urban environments where measurement and
160 installation conditions are sometimes complicated. More than twenty IoT stations (DecentLab
161 DL-SHT35-001 - air temperature and humidity sensor with radiation shield for LoRaWAN) have
162 been installed in central Paris starting in July 2022. These are compact and lightweight
163 stations installed on lampposts at a height of approximately 5 m AGL, following the
164 recommendations made by Oke (2006). The stations have been installed on the north side of
165 the lampposts to limit sensor warming through solar irradiance. The reference built-up setting
166 temperature is computed as the average temperature recorded by four IoT stations located
167 within 500 m of each other, in the highly urbanised neighbourhood of the Paris Opera House
168 (hereafter referred to as Opera). Note that these stations were operational only from July 8,
169 2022. For the period prior to this date (1 June to 7 July), the built-up setting temperature is



170 derived from the Météo France weather station Lariboisière Hospital (10th district of Paris)
171 which is located 2 km northeast of the Opera neighbourhood in an equally dense built-up
172 setting. Comparisons of temperatures measured at Lariboisière and Opera during July and
173 August 2022 do not reveal any significant differences (not shown). The built-up setting
174 temperature (at Lariboisière and Opera) is considered not influenced by green space cooling,
175 as the closest urban park is about 1 km away and cooling effect distances of parks reported
176 in the literature are far less than 1 km (Aram et al. 2019).

177

178 Finally, we used temperature and wind speed and direction measured at the top of the Eiffel
179 Tower (287 m AGL) to monitor conditions at a height generally located in the nocturnal urban
180 boundary layer.

181

182 **i) Doppler Wind Lidar**

183 A Doppler Wind Lidar (DWL) is used in this study to deduce the intensity of vertical turbulent
184 mixing. The Vaisala DWL WindCube Scan 400 was installed at 90 m above ground level (AGL)
185 at the top of the Zamansky Tower located on the campus of Sorbonne University in the 5th
186 district of Paris (QUALAIR atmospheric station location shown on Fig. 1; <https://qualair.fr/>) to
187 measure horizontal wind and vertical velocity. In this study, we use vertical-stare mode of
188 the DWL to derive vertical velocity variance (σ_w) profiles. Each variance profile is calculated
189 from 300 vertical velocity profiles collected during a 5-min period (one profile per second).
190 Vertical velocity variance profiles are available every 30 minutes. Due to installation setup,
191 the first gate available for deriving the vertical velocity variance is at 238 m AGL.

192

193 **ii) Windsond**

194 A Windsond is a lightweight sonde (12 grams) manufactured by Sparv Embedded, Sweden
195 (<https://sparvembedded.com/products/windsond>). This instrument, packaged in a styrofoam
196 cup, records pressure, temperature, and relative humidity approximately every second.
197 Latitude and longitude are determined using an onboard GPS receiver. The S1H3 windsond
198 model calculates wind speed and direction independently from latitude and longitude,
199 utilising the GPS signal. Thanks to its lightweight design, the balloon size is somewhat

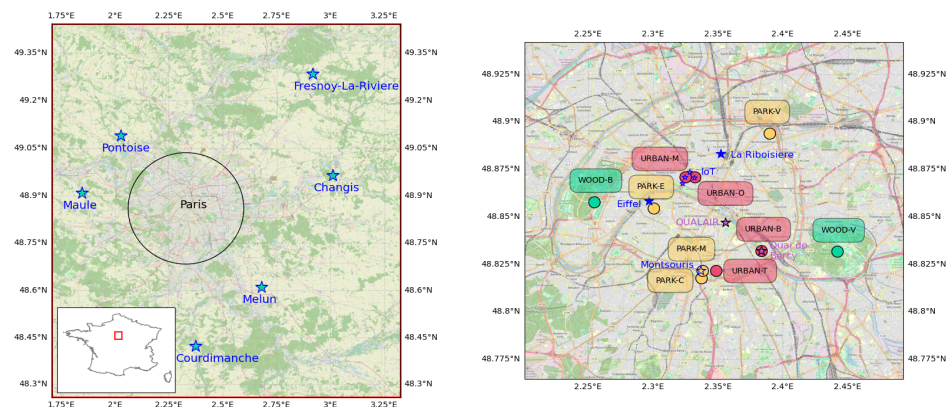


200 equivalent to a "party balloon", requiring about 50 L of helium, and making it particularly
201 suitable for probing the lower parts of the troposphere.

202 For each IOP, three profiles were produced using windsonds to monitor evening cooling at
203 16, 20 and 00 UTC. The 16 UTC profile corresponds to conditions of maximum daytime
204 temperatures. The 20 UTC profile samples conditions about 1 hr after sunset, while the 00
205 UTC profile is performed in conditions close to the maximum nighttime UHI.

206 Corrections have been applied to raw data as follows. Before the windsond is released, the
207 temperature and humidity sensors are not ventilated. Unventilated data (before launch) are
208 thus carefully compared with the first points of the ventilated profile, and corrected if
209 necessary. As the temperature and humidity sensors are outside the styrofoam cup, the
210 windsond is subject to the influence of solar radiation during the day. A daytime overheating
211 on the order of about +1°C was observed by comparing those profiles with data collected by
212 Vaisala RS41-SGP radiosondes launched at the same time the URBAN-B location (see
213 Appendix 1). A correction of -1°C was therefore applied across the entire profile for
214 windsonde data at 16 UTC. No radiative correction is applied at 20 and 00 UTC.

215



216

217 Figure 1: (left) Locations of the six weather stations contributing to the rural setting
218 reference. (right) Locations of fixed weather stations in Paris city (blue stars) and of
219 windsond and radiosonde launch sites in urban woods (green dots WOOD), urban
220 parks (yellow dots PARK) and built-up areas (red dots URBAN). © OpenStreetMap
221 contributors 2023. Distributed under the Open Data Commons Open Database
222 License (ODbL) v1.0.

223



224

225

226 2.2 Sampling methodology

227

228 Our study focuses on evening temperature evolution at various locations across the Paris
229 region under predominantly cloud free conditions. The cloud cover fraction is derived on an
230 hourly basis using a Lufft CHM15k automatic lidar ceilometer located at the SIRTA observatory
231 (Haefelin et al. 2005) and a second one located at the QUALAIR atmospheric station. Evening
232 cloud-free conditions are defined as a cloud fraction less than 20% for each hour between 16
233 and 00 UTC. In the period June-August 2022, 54 days are classified as “evening cloud-free
234 conditions”.

235

236 The 14 intensive observation days were selected to focus predominantly on warm to hot
237 daytime conditions followed by cloud free nights. Two heat wave events were covered with
238 intensive observations, the first one on 16-18 June and the second one on 12-19 July.

239 Windsond launch sites were classified in three types of settings i.e. urban woods, urban parks
240 and built-up areas. Two urban woods, located East of the city (Bois de Vincennes, 995 ha;
241 WOOD-V in Fig. 1) and West of the city (Bois de Boulogne, 845 ha; WOOD-B), are mostly
242 wooded, including open lawns, small lakes, buildings and roads. Three urban parks of
243 comparable size were selected to sample different neighbourhoods of the city. One is located
244 south of the city centre (Cité Universitaire about 32 ha with 50% green space and 50%
245 housings and small roads, located across the street from Montsouris Park; PARK-C), the
246 second one is West of the city centre (Eiffel Tower park, 24 ha, predominantly trees and open
247 lawns; PARK-E), and the third one is Northeast of the city centre (La Villette Park, 55 ha
248 including 30 ha of green space and 25 ha of built-up areas; PARK-V). Windsonds were also
249 launched from four built-up areas: one in the 13th district close to Montsouris Park (URBAN-T
250 in Fig 1.), two in the 9th district close to the Opera IoT stations (URBAN-M and URBAN-O), and
251 one in the 12th district next to the radiosonde launch site (URBAN-B). For the June 3-day heat
252 wave, we sampled one park, one wood and one built-up site. For the July heat wave, we were
253 able to sample the three parks, two woods and two built-up sites. Launch sites are shown in
254 Fig. 1 and IOP dates and launch locations are shown in Table 1.



276 same built-up environment and the vegetated rural reference. The study covers summer 2022
277 focusing on the 54 evening periods with cloud-free conditions (defined in Section 2).
278

279 3.1 Summertime urban park cooling effect variability

280 The regional UHI is known to be dependent on both cloud-cover fraction and wind speed.
281 Here we focus on cloud-free nights, for which the UHI has been found to be proportional to
282 the inverse of the square-to-third root of the wind speed (e.g. Morris et al. 2001). Cespedes
283 et al. (2024) has also shown that the strongest UHI intensities are found for very low vertical
284 velocity variance values, measured above the urban canopy, and that UHI decreases as
285 vertical velocity variance increases.

286 Fig. 2 presents median nocturnal cooling intensity of the Montsouris Park (a 15-ha urban park)
287 against the median nocturnal regional UHI and median vertical velocity variance computed
288 over the 19-02 UTC time interval for each night. A K-means clustering method based on the
289 three variables is used to identify different regimes. The figure reveals three different
290 regimes. In conditions of strongest UHI (6-10°C), we find a group of days where the park
291 cooling effect intensity ranges 2-5°C. In this regime, the vertical velocity variance is very low
292 with median nocturnal values ranging from 0.02 to 0.1 m²s⁻². In these conditions, urban park
293 cooling intensity relative to the built-up environment shows a strong variability, but is on
294 average half the regional UHI intensity. In conditions of weak UHI intensity (2-4°C), the park
295 cooling effect is close to 1°C, while the vertical velocity variances are high (greater than 0.25
296 m²s⁻²). In this regime, intra-urban temperatures are most homogeneous and urban-rural
297 contrasts are minimal, which is likely due to significant advection. In between, we find a
298 number of days where the urban park cooling effect remains limited (1-2°C), while the urban-
299 rural temperature contrasts are significantly stronger (4-8°C), by a factor of about four. In
300 these conditions, we find that the vertical velocity variances range between 0.1 and 0.2 m²s⁻².
301 For those days, the rural environment around the city cools very efficiently, while the urban
302 setting remains hot with little intra-urban contrasts.

303 In summary, we can state that:

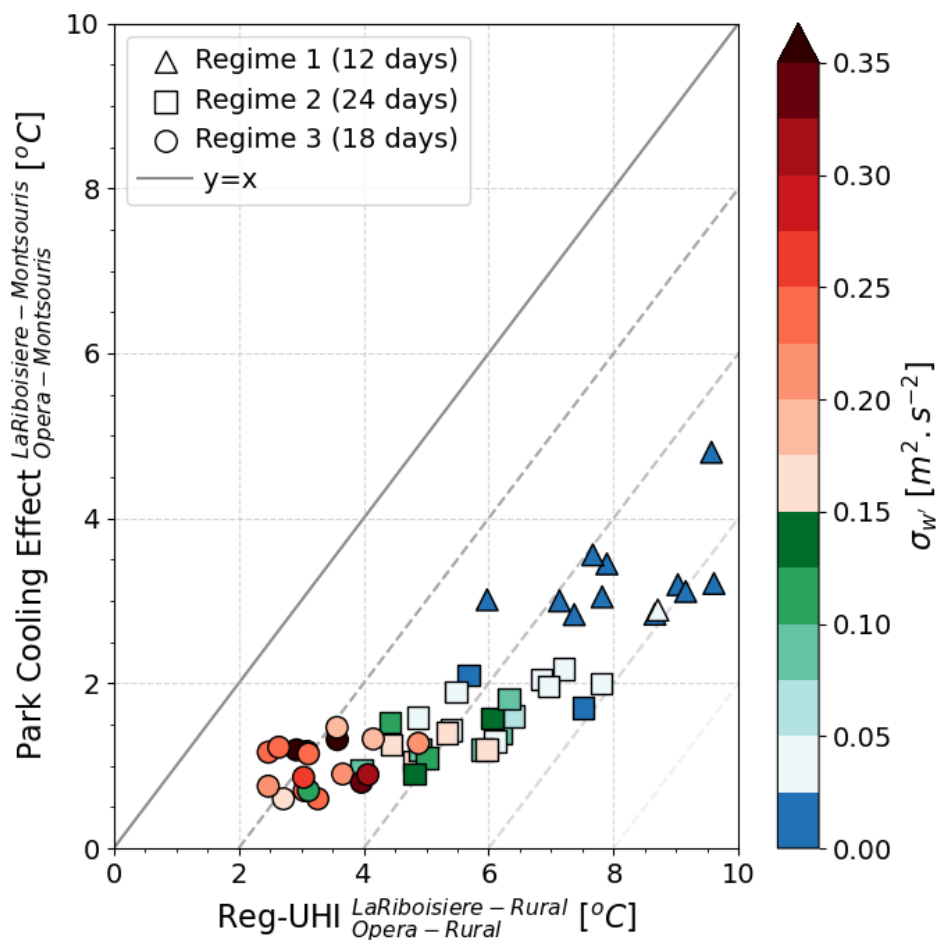


- 304 • Conditions of strong park cooling intensity combined with strong regional UHI
305 intensity occur in a regime of low vertical velocity variance. This regime will be referred
306 to as the stagnant regime in the rest of the paper,
- 307 • Conditions of moderate park cooling intensity combined with strong regional UHI
308 intensity occur in a regime of moderate vertical velocity variance (referred to as the
309 intermediary regime).
- 310 • conditions of weak park cooling intensity combined with weak regional UHI intensity
311 occur in a regime of high vertical velocity variance (referred to as the turbulent
312 regime).

313 Based on these findings, several questions arise. What processes drive the evening cooling in
314 the urban park in these different conditions? What is responsible for the different urban park
315 cooling effects that we find for low, moderate and high vertical velocity variance?

316

317



318

319 Figure 2. Nocturnal urban park cooling effect intensity against regional-scale UHI intensity and
320 vertical velocity variance (color scale), derived from 8 hours of measurements (median 19-02
321 UTC values) for the 54 cloud-free evenings.

322

323 3.2 Urban park cooling effect variability in a heatwave period

324

325 To better understand factors affecting the variability in nocturnal temperature contrasts
326 between urban parks and the built-up settings, we focus next on an eight-day event (12-19



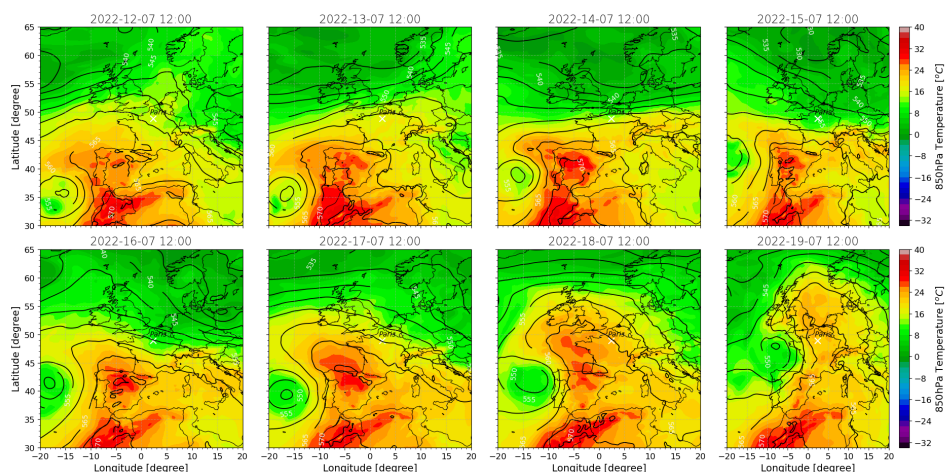
327 July 2022) that is characterised by extreme daytime temperature (peak values approaching
328 40°C on several days) and a set of diverse evening cooling patterns.

329

330 This period is characterised by a powerful anticyclonic axis between Morocco, France and the
331 British Isles, which gradually warmed the air (Fig. 3). A secondary low-pressure system located
332 between the Azores and Portugal moved towards the Bay of Biscay, strengthening the
333 advection of particularly hot air from the Iberian Peninsula. This contributed to the
334 intensification of a heatwave over the European continent, with an extreme peak over the
335 Paris region on July 19. As it moved north-eastwards over France, this low pressure system
336 advected cooler oceanic air from the west, causing temperatures to fall and progressing
337 eastwards with thunderstorm activity. During the heatwave, the 850 hPa temperature
338 exceeded 20°C, while on standard summer days, it is closer to 10°C.

339

340



341

342 Figure 3: Synoptic overview from 12 to 19 July 2022 based on ERA5 reanalysis. The colour
343 bar represents temperature at 850 hPa, and the contours represent the geopotential height
344 difference between 500 hPa and 1000 hPa (dam).

345

346 Figure 4 shows the temporal evolution of near-surface atmospheric conditions during the
347 eight-day period. Figure 4a compares the 2-m air temperature measured in Opera built-up
348 setting, Montsouris urban park, and the rural reference setting. The regimes identified in
349 Section 3.1 are also shown for each night. Figure 4b presents the rate of change of



350 temperature over time at the three locations. Figure 4c shows the temperature differences
351 between the built-up site and the urban park and the rural setting, respectively. Figure 4d
352 presents the wind speed and direction measured at the Montsouris urban park 25 m AGL and
353 Fig. 4e shows the vertical velocity variance measured at 240 m AGL.

354

355 The eight-day period is characterised by a first heat wave on July 12 and 13 (stagnant regime),
356 due to the advection of hot air shown in Fig. 3, with maximum temperature exceeding 35°C,
357 followed by three days of more moderate heat on July 14, 15, and 16 (intermediary and
358 turbulent regimes, maximum temperature at or below 30°C and minimal temperatures in the
359 built-up environment less than 20°C). A second, more intense, advection of hot air occurs the
360 following three days on July 17, 18, and 19 (stagnant regime) with daytime maximum
361 temperatures exceeding 35°C. Figure 4a shows that the daytime maximum temperatures
362 (between 16 and 17 UTC) in the built-up, urban park and rural settings are close, within 1°C
363 of each other. Conversely, night-time minimal temperatures (between 03 and 04 UTC) differ
364 by 4-10°C between the built-up and rural settings with significant day to day variations (Figure
365 4c).

366

367 Figure 4b shows positive heating rates from sunrise until about one hour before sunset. Peak
368 heating rates reach 2-3°C/hr, but are on average near 1°C/hr. One hour before sunset,
369 temperature changes become negative (cooling). We observe a two-phase cooling consistent
370 with earlier findings reported in the literature (e.g. Holmer et al. 2013). The first phase lasts
371 from 16 to 21 UTC. It is characterised by large changes in cooling rate reaching maximum
372 values near 19-20 UTC and with differences of up to 2°C/hr between built-up, urban park, and
373 rural cooling rates (on 12/07, 17/07 and 18/07). The second phase starts after 21 UTC and
374 lasts until sunrise or about 04 UTC. It is characterised by more moderate cooling rates of
375 typically less than -1°C/hr and by virtually no contrasts between built-up, park and rural
376 settings.

377

378 In the evening, air temperature cooling in the urban canopy is driven by a combination of
379 processes, including radiative cooling of the surfaces and the air (through radiative flux
380 divergence), turbulent heat exchange (through sensible and latent heat fluxes), release of
381 heat from the ground (storage heat flux), vertical mixing of air, and advection (Oke 2017).



382 These processes are known to depend on the surface types and properties (albedo, emissivity,
383 heat capacity, soil moisture), the 3-D canopy structure (sky view factor), the city morphology,
384 anthropogenic heat emissions, the spatial distribution of surface types (urban to rural surface
385 gradients), and synoptic-scale weather conditions (wind, clouds). According to Steeneveld et
386 al. (2006), atmospheric static stability and mesoscale dynamics affect the relative contribution
387 of the radiative and turbulent processes. When the vertical turbulent mixing is low, turbulent
388 heat fluxes are weak, hence air temperature cooling is dominated by radiative flux divergence,
389 partially compensated by the storage heat flux.

390

391 This is consistent with cooling rates shown in Fig. 4b. In the rural setting and in the urban park,
392 where the storage heat flux is low, the largest cooling rates (peaking at $-3^{\circ}\text{C}/\text{hr}$ and $-2^{\circ}\text{C}/\text{hr}$
393 respectively) are observed in conditions of low vertical velocity variance (Fig. 4e), on the
394 evenings of 12/07, 17/07 and 18/07 (stagnant regime). In the built-up area, the radiative
395 cooling is partially compensated by a stronger ground heat flux. On nights with moderate to
396 high vertical velocity variance, radiative flux divergence is reduced and also compensated by
397 sensible and latent heat flux releases, which leads to lower cooling rates in both urban park
398 and rural settings. The excess of urban-park cooling compared to the built-up environment
399 lasts four to six hours (from 18 to 00 UTC) as is the case for the rural surface.

400

401 The contrasts in cooling rates between the built-up environment, the urban park and the rural
402 settings can explain the large variability in nocturnal park cooling effect and regional-scale
403 UHI intensities shown in Fig. 4c. On the three nights with lowest wind speed ($<2\text{ m s}^{-1}$, Fig. 4d)
404 and lowest vertical velocity variance ($<0.05\text{ m}^2\text{ s}^{-2}$), that is on 12-13/07, 17-18/07 and 18-
405 19/07 (stagnant regime), the maximum regional UHI intensity exceeds 8°C , while the
406 maximum park cooling effect reaches nearly 4°C . On those nights, in the built-up
407 environment, the air temperature cools by $7\text{-}9^{\circ}\text{C}$ from sunset to sunrise, while the urban park
408 cools an extra $3\text{-}4^{\circ}\text{C}$, and the rural setting an additional $3\text{-}4^{\circ}\text{C}$. On the night with moderate
409 wind speed ($3\text{-}4\text{ m s}^{-1}$) and moderate vertical velocity variance, 15-16/07(intermediary
410 regime), the regional UHI peaks near 6°C , while the park cooling effect reaches about 2°C . On
411 this night, the air temperature cools by about 10°C from sunset to sunrise in the built-up
412 environment, while the urban green infrastructure cools an extra 2°C , and the rural setting an
413 additional $3\text{-}4^{\circ}\text{C}$. On the nights of 14-15/07 and 16-17/07 (turbulent regime), the wind speed

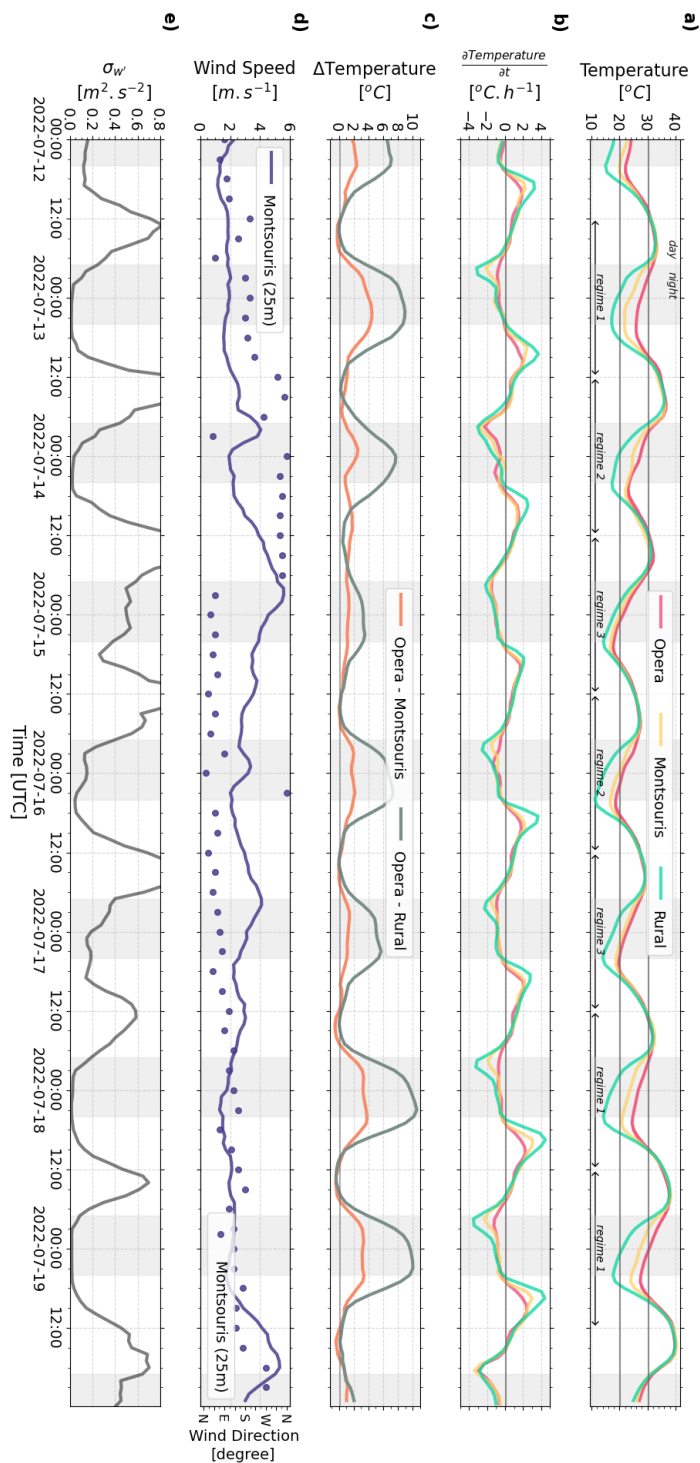


414 exceeds 4 m s^{-1} and the park cooling effect reaches just 1°C , while the maximum regional UHI
415 intensity is about 4°C .

416

417 The analysis of the 12-19 July period confirms the results shown in Fig. 2. Different regimes
418 exist that influence park cooling effect and regional UHI intensities. In particular, during nights
419 with very low wind speeds, the air above the urban park cools significantly more (up to 4°C)
420 than in our reference built-up environment. To better understand the processes and
421 conditions that affect these nocturnal intra-urban cooling contrasts we will investigate the
422 dynamics and thermodynamics of the urban boundary layer over green infrastructures of
423 different sizes in the following section.

424





426 Figure 4: near-surface temperature and nighttime turbulence regimes (a) and cooling rate (b)
427 measured in a built-up environment (Paris Opera district), an urban park (Montsouris park,
428 15-ha), and the average of 6 rural locations around Paris; Urban park cooling effect (Opera-
429 Montsouris temperature difference) and regional-scale UHI (Opera-Rural temperature
430 difference) (c); wind speed and direction measured at Montsouris Park 25 m AGL (d); and
431 vertical velocity variance measured in Paris city centre 238 m AGL. 12-19 July 2022; during
432 that week, the sun sets at about 19 UTC and rises at about 04 UTC.
433

434 4) Evening cooling in and above urban parks and 435 urban woods

436
437 In this section, we focus on four different nights to study the characteristics of evening cooling
438 mechanisms above urban green spaces considering dynamics of the urban boundary layer for
439 the three turbulence regimes. For each evening period (16-00 UTC), we analyse time series of
440 near-surface temperature, humidity, and wind measured in the built-up environment, urban
441 green infrastructures, and rural settings. To investigate the relative role of relevant cooling
442 mechanisms, i.e. radiative cooling of the surfaces, radiative cooling of the air through
443 radiative flux divergence, turbulent heat exchange, vertical mixing, and advection, it is helpful
444 to quantify conditions in the urban boundary layer. Therefore, in order to assess the relative
445 roles of surface-driven and atmospheric-driven processes, the conditions measured at the
446 surface are complemented by the analysis of the observations at the top of the Eiffel Tower
447 (287 m AGL), as well as vertical profiles of meteorological variables obtained from windsound
448 profile measurements.
449

450 4.1 Stagnant regime: strong park cooling effect combined with 451 strong UHI intensity

452



453 Here we focus on two nights that show the strongest park cooling effect intensity and most
 454 significant UHI intensity, classified as stagnant regime, i.e. 12-13/07 and 17-18/07. Both
 455 selected nights occur in high-pressure synoptic conditions with meso-scale subsidence over
 456 the region. Hot air advection driven by a secondary pressure low located west of the Iberian
 457 Peninsula led to 850 hPa temperatures near 20°C. Both nights are characterised by very warm
 458 conditions over the preceding daytime period with daily maximum air temperatures
 459 exceeding 32°C (see Fig.s 5a, 6a). Strong regional-scale UHI and park cooling intensities are
 460 due to sharp contrasts in peak cooling rates (Fig.s 5b and 6b) between built-up, park and rural
 461 settings that last for 4-6 hours. On both 12/07 and 17/07, an evening cooling (16-00 UTC) of -
 462 5°C, -9°C and -14°C is documented in the built-up, urban park and rural settings, respectively,
 463 as shown in Table 2.

464

	16-00 UTC cumulative temperature change [°C] (average cooling rate [°C/h])		
Regimes	Opera	Park	Rural
Stagnant Regime : Strong park cooling effect and strong UHI intensities	-5.1 (-0.6)	-9.1 (-1.1)	-14.0 (-1.8)
Intermediary Regime: Moderate park cooling effect and strong UHI intensities	-5.9 (-0.7)	-7.6 (-0.9)	-12.6 (-1.6)
Turbulent Regime: Weak park cooling effect and low UHI intensities	-9.6 (-1.2)	-9.4 (-1.2)	-13.1 (-1.6)

465 Table 2: 16-00 UTC cumulative evening temperature change and average cooling rate for the
 466 three turbulence regimes.



467

468 The relatively strong cooling rate in the urban park compared to the built-up settings suggests
469 that the surface-driven processes (i.e. radiative cooling and/or turbulent latent heat fluxes)
470 are rather efficient on those nights. In comparison, the air temperature at the top of the Eiffel
471 Tower peaks generally around 18 UTC, i.e. about 2 hr later than near the surface at values 2-
472 3°C colder than the near-surface air temperature (Fig.s 5a and 6a). After 18 UTC, the air starts
473 to cool with a rate of around -0.35°C/hr, which is nearly half the value of the near-surface
474 cooling rate measured in the built-up environment (Fig.s 5b and 6b). Hence, the air at 287 m
475 AGL is only moderately affected by the processes that cool the air close to the surface. This is
476 the first evidence of decoupling between the urban canopy layer (UCL) and the air above, and
477 the decrease in static instability in the urban boundary layer (UBL).

478

479 Further evidence of this decoupling due to static stability in the UBL can be found in the wind
480 speed measurements. Figures 5c and 6c show the time series of wind speed at 10 m AGL at
481 the Melun rural site, at 25 m AGL in the Montsouris urban park and at 287 m AGL at the Eiffel
482 Tower, for 12/07 and 17/07, respectively. A comparable temporal evolution of wind speed
483 can be observed in the evening hours on both days. During the afternoon, the wind speed at
484 both the urban park and the rural site are consistent (about 2-4 m s⁻¹ and within 1-2 m s⁻¹ of
485 each other). After about 18 UTC, the wind speed at 287 m AGL increases rapidly to reach 8-
486 10 m s⁻¹ before 00 UTC, while the rural and urban park wind speed remains low at or below 2
487 m s⁻¹, i.e. often lower than during daytime. This is a second evidence that after sunset,
488 decoupling conditions occur between the surface layer and the air above.

489

490 Figures 5 and 6 g and h show vertical profiles of wind speed and direction derived from
491 windsound profiles launched at 16, 20 and 00 UTC over an urban park (PARK-E; Fig. 1) on 12/07
492 and a large urban wood (WOOD-B; Fig. 1) on 17/07, respectively. Both IOPs are characterised
493 by easterly winds with relatively little wind direction evolution in the evening. During daytime
494 (16 UTC), the wind speed is moderate (2-4 m s⁻¹) in the first 700 m of the atmospheric
495 boundary layer. The windsounds launched after sunset (near 20 UTC) reveal in both cases low
496 near-surface wind speed (1.5-2.0 m s⁻¹) that gradually increases with height (consistent with
497 results described in the previous paragraph). A 3 m s⁻¹ wind shear can be observed on 17/07
498 between the surface and 200 m AGL. The wind shear is not as strong on 12/07, possibly



499 because the profile was measured 45 min earlier than on the other day. This wind shear is a
500 signature of the stabilisation of the atmosphere that inhibits the vertical transfer of
501 momentum and hence decouples the air aloft from surface drag effects, allowing the wind
502 speed to increase aloft (e.g. Barthelemie et al. 1996).

503

504 The windsonds launched at 00 UTC reveal even stronger windshear between surface and 200
505 m AGL, with maximum wind speed of around 6.5 m s^{-1} on both nights near 300 m AGL and a
506 decreasing wind speed above. This vertical structure is known as a low-level jet (LLJ), a
507 condition that occurs frequently on summer nights above Paris according to Céspedes et al.
508 (2024). Their work has shown that very low altitude LLJs are associated with low levels of
509 turbulence, due to the fact that they form in a statically stable atmosphere that inhibits
510 mechanically induced turbulence.

511

512 To characterise the importance of vertical mixing as a potential means for heat transfer
513 between the UCL and the nocturnal urban boundary layer, we use Doppler wind lidar
514 measurements to derive time series of vertical velocity variance (Figs 5d and 6d). During the
515 convective period of the two IOPs, the vertical velocity variance typically exceeds $0.5 \text{ m}^2 \text{ s}^{-2}$. It
516 then decreases rapidly around sunset. At 20 UTC, the values have dropped to less than 0.05
517 $\text{m}^2 \text{ s}^{-2}$ on both 12/07 and 17/07, and remain very low all night. This confirms the very low
518 vertical turbulent mixing in the UBL on both nights.

519

520 To characterise the role of vertical radiative flux divergence in the atmospheric boundary
521 layer, and to better understand the relative importance of surface-driven vs atmospheric-
522 driven processes, we analyse the vertical structure of temperature and its temporal evolution.
523 In the Eiffel Tower urban park (PARK-E), we find that near-surface temperatures measured by
524 the windsond on 12/07 are consistent with temperatures recorded by the Montsouris urban
525 park surface station (yellow circles in Fig. 5a). At 20 UTC, we observe a 1°C temperature
526 inversion between the surface and 50 m AGL (Fig. 5f). Above the inversion, the temperature
527 decreases adiabatically by about $-1^\circ\text{C}/100 \text{ m}$ so that the potential temperature is nearly
528 constant in a statically neutral layer between 50 and 700 m (Fig. 5f). At 00 UTC, the surface-
529 based inversion has become stronger ($\Delta T_{\text{air}} = 2.5^\circ\text{C}$ and $\Delta \theta_{\text{air}} = 3.0^\circ\text{C}$ between the surface and



530 50 m AGL), and two elevated inversions have formed near 100 and 200 m AGL (Fig. 5f, g), with
531 $\Delta\theta_{\text{air}} = 0.5^{\circ}\text{C}$ followed by a statically stable layer with a $+0.2^{\circ}\text{C}/100\text{ m}$ lapse rate (Fig. 5g).

532

533 In the urban wood (WOOD-B), near-surface temperatures measured by the windsound on
534 17/07 are close to temperatures measured in the rural settings (green circles in Fig. 6a). With
535 3.5°C decrease over 50 m, the surface-based temperature inversion at 20 UTC (Fig. 6e) is
536 already stronger than the inversion observed at 00 UTC over PARK-E on 12/07. Above the
537 inversion, the temperature decreases adiabatically (Fig. 6e, f) and the potential temperature
538 profile confirms that the stable wood UBL is capped by a neutral layer above. At 00 UTC, the
539 surface-based inversion strengthens and extends aloft ($\Delta T_{\text{air}} = 5.0^{\circ}\text{C}/100\text{ m}$; $\Delta\theta_{\text{air}} = 6^{\circ}\text{C}/100$
540 m), followed by an elevated inversion near 250 m AGL (Fig. 6f, g). The potential temperature
541 profile is stable between 100 and 300 m AGL ($+1.0^{\circ}\text{C}/100\text{ m}$) and moderately stable
542 ($+0.2^{\circ}\text{C}/100\text{ m}$) above (Fig. 6g).

543

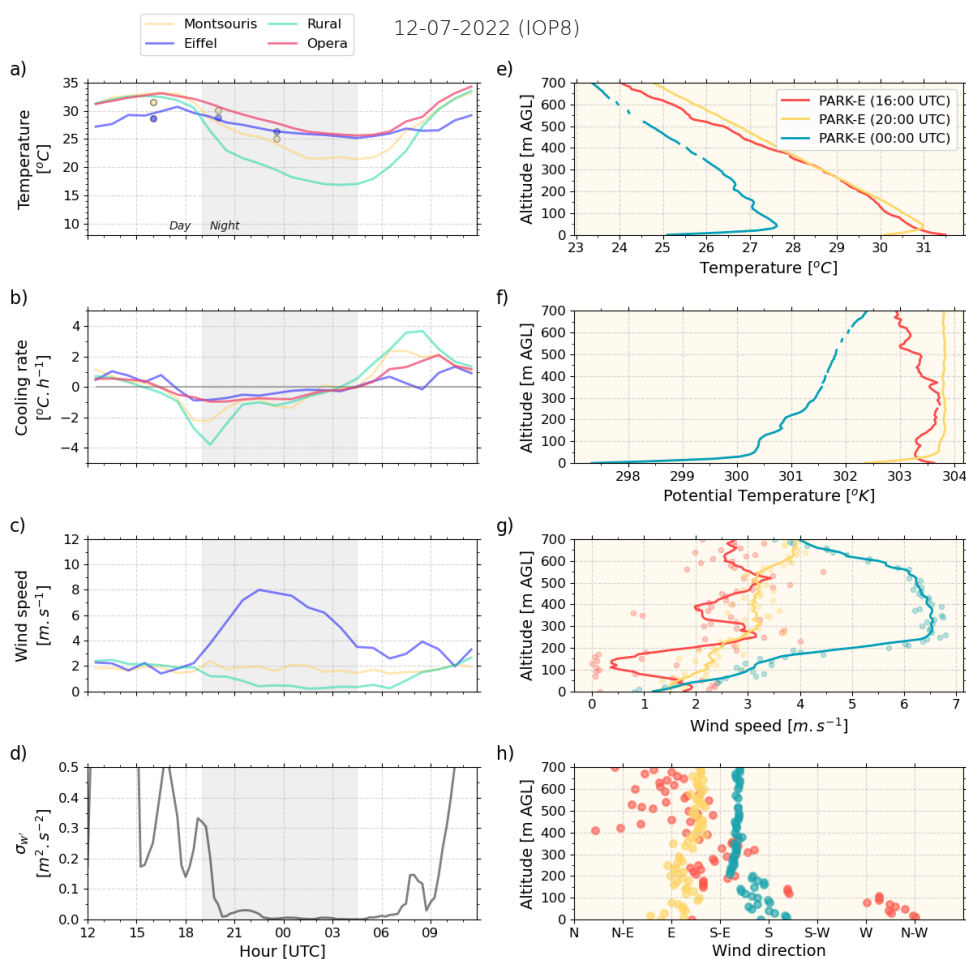
544 These elevated inversions observed both over the urban park and urban wood could be
545 formed through localised radiative cooling, subsidence and/or advection of statically stable
546 rural air that is commonly observed above nocturnal UBL (e.g. Tsiringakis et al. 2022). Elevated
547 inversions in nocturnal UBLs are simulated and studied extensively in Martilli (2002). The drag
548 and turbulent kinetic energy production induced by the urban structure increases with
549 increasing wind speed. Vertical mixing of potential temperature leads to a local minimum of
550 temperature at the location of maximum turbulence through a negative turbulent heat flux.
551 According to Martilli (2002), the net result of the vertical turbulent transport is to heat the
552 layer below the base of the inversion and to cool the inversion layer. Cooling of the inversion
553 layer (roughly between 200 and 300 m AGL) is clearly seen on the both windsound temperature
554 profiles measured at 00 UTC.

555

556 We can conclude that the conditions of stagnant regime, combining strong park cooling
557 effects and strong UHI intensities, are associated with a significant surface-based inversion
558 that leads to the decoupling not only of the rural nocturnal boundary layer from the residual
559 layer but also between the urban boundary layer and the neutral layer above. The strong
560 stratification suppresses nearly any turbulent vertical motion so that the UBL height is rather
561 shallow - even below the top of the Eiffel Tower. As the flow is no longer subject to surface



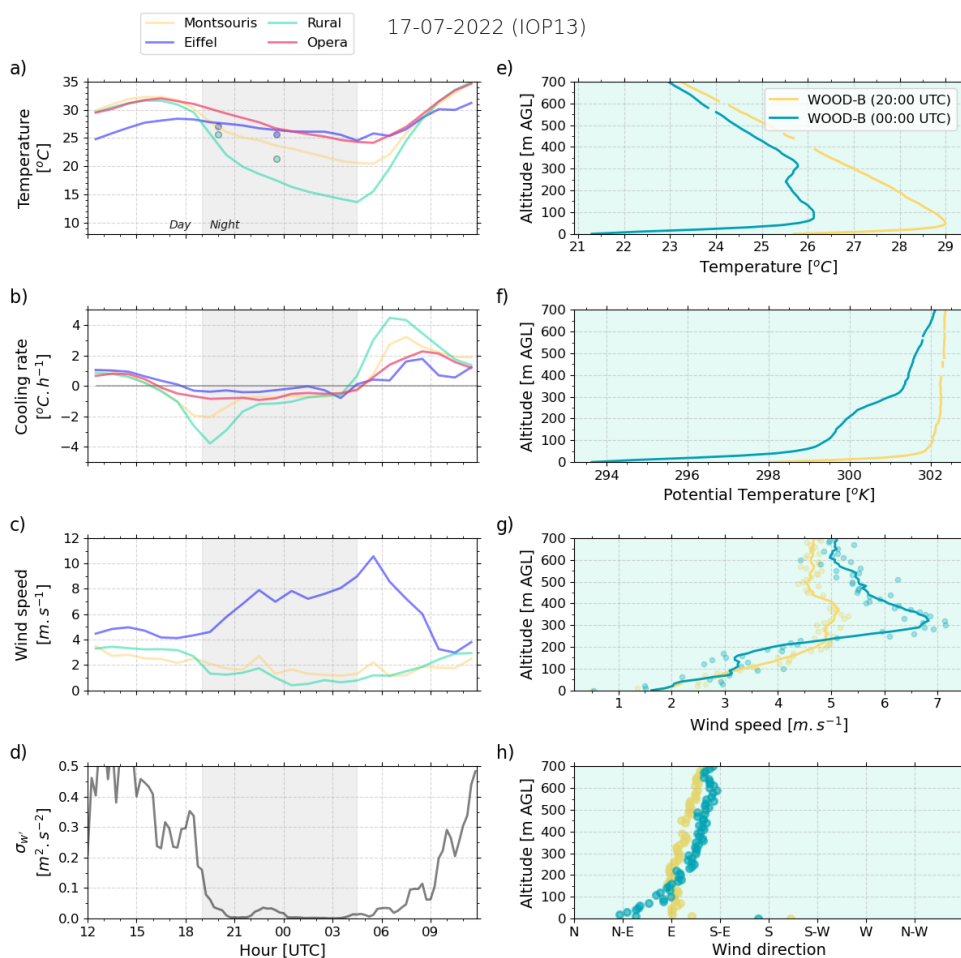
562 drag, a regional low-level jet forms that likely advects rural, statically stratified air over the
 563 UBL, which can influence the development of elevated inversions. The strong stratification in
 564 the park internal UBL is the result of cooling dominated by radiative flux divergence due to
 565 low turbulent mixing.
 566
 567



568
 569 Figure 5: Time series and windsonde profile measurements for July 12, 2022. a-d) Time series
 570 measurements from 12 UTC to 12 UTC (D+1). a) Temperature at Montsouris Park, Rural
 571 settings, Opera (built-up) and top of Eiffel Tower. The coloured dots show the temperature
 572 measured by windsonds at 16, 20, and 00 UTC, respectively at park level and at the height of
 573 the Eiffel Tower (287m AGL). b) Cooling rate at Montsouris, Rural, Opera and Eiffel Tower. c)
 574 Wind speed at Montsouris, Rural, and Eiffel Tower. d) Vertical velocity variance from DWL at



575 238 m AGL at QUALAIR-SU site. e-h) Vertical profiles from radiosonde measurements
576 released in PARK-E at 16, 20, and 00 UTC, respectively. e) Temperature profile. f) Potential
577 temperature profiles. g) Wind speed profiles. h) Wind direction profiles.
578



579

580 Figure 6: same as Fig. 5 for July 17, 2022.

581

582

583

584

585

586

587

588



589

590

591

592 4.2 Intermediary regime: moderate park cooling effect

593 combined with strong UHI intensity

594

595 The evening of 15-16/07, compared to those discussed in Section 4.1, is characterised by
596 weaker cooling between 16 and 00 UTC in the rural setting and urban park, and stronger
597 cooling in the built-up environment, as shown in Table 2. It is classified in the intermediary
598 regime. Cooling peaks near $-3^{\circ}\text{C}/\text{hr}$ in the rural setting and $-1.5^{\circ}\text{C}/\text{hr}$ in urban park, which is
599 slightly less than for the cases of Section 4.1 (Fig. 7b). For this regime, the nocturnal near-
600 surface wind only decreases in the rural setting while it increases in the urban park after 21
601 UTC as the wind aloft picks up (Fig. 7c) which indicates that vertical momentum transfer is
602 less inhibited above the urban surface. Figure 7d shows that the vertical turbulent mixing
603 remains above $0.1\text{ m}^2\text{ s}^{-2}$ after sunset and increases to $0.2\text{ m}^2\text{ s}^{-2}$ during the evening which
604 confirms that the UBL remains turbulent during the night.

605

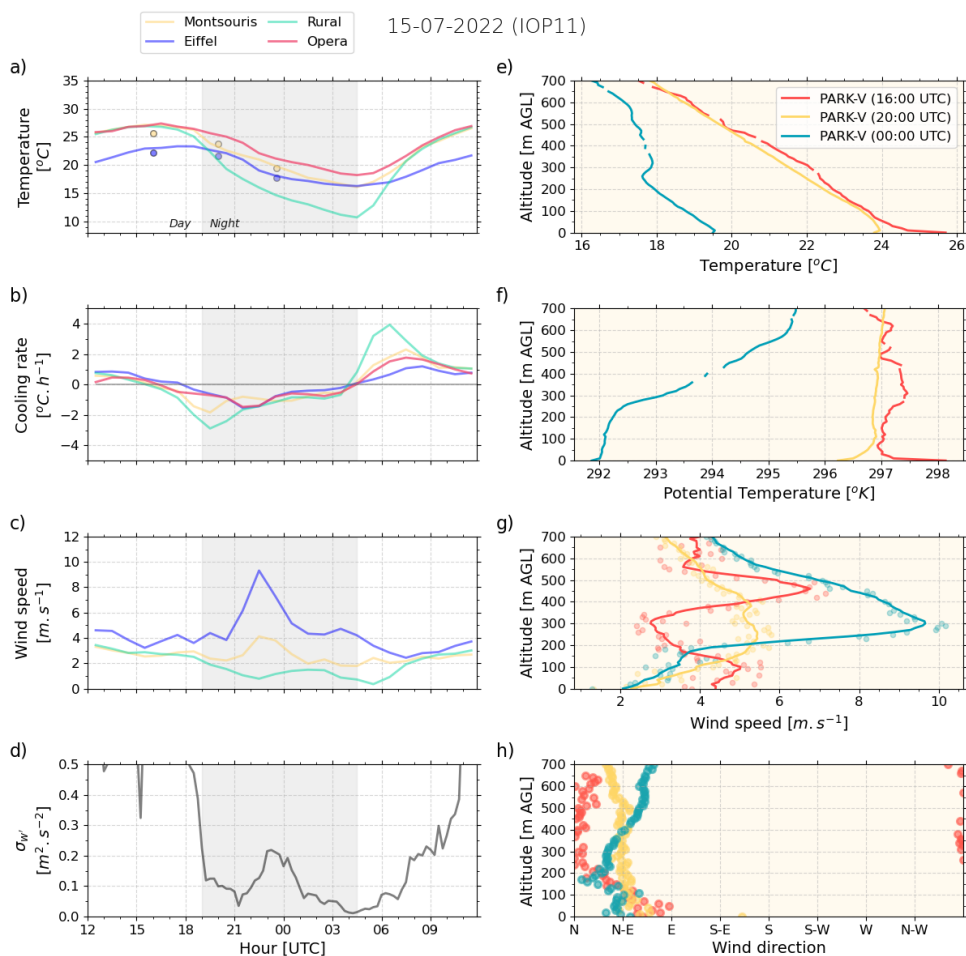
606 The windsound profiles carried out in the La Villette urban park (PARK-V on Fig. 1), for which
607 the vegetated area is comparable to that of the Montsouris urban park, reveal at 20 UTC a
608 slight surface-based inversion with a neutral layer above, while at 00 UTC under brisker
609 turbulent mixing the UBL remains near-neutral from the ground up to a temperature
610 inversion near 300 m AGL. It is then likely that the UBL remains neutral due to sensible heat
611 fluxes originating from the hot surface combined with turbulent mixing and from the
612 temperature inversion above. Again, a clear low-level jet with peak horizontal velocity $> 9\text{ m}$
613 s^{-1} near the height of the temperature inversion suggests that stably stratified air from rural
614 surroundings is advected over the city.

615

616 The intermediary regime highlights that while the rural nocturnal layer becomes statically
617 stable during the evening, as evidenced by the very low near-surface wind speed at the rural



618 site, the UBL remains statically neutral. Vertical turbulent mixing in the UBL prevents a
 619 temperature inversion to form in the UCL, even above the urban green space.
 620



621
 622 Figure 7: same as Fig. 5 for July 15, 2022 (IOP11)

623
 624
 625
 626
 627
 628
 629



630 4.3 Turbulent regime: weak park cooling effect combined with
631 weak regional UHI intensity

632

633 The evening of 04/07, classified in the turbulent regime, is characterised by nearly identical
634 cooling rates in built-up settings, urban green spaces, as well as aloft at the top of the Eiffel
635 Tower. Cooling peaks near -2 to $-2.5^{\circ}\text{C}/\text{hr}$ at all locations (Fig. 8b). Wind speed at both the
636 rural settings and the urban park does not decrease after sunset, but rather increases after
637 18 UTC as the wind aloft picks up (Fig. 8c). In addition to the strong advection effects, the UBL
638 remains turbulent during the night as turbulent vertical mixing remains above $0.2\text{ m}^2\text{s}^{-2}$ after
639 sunset (Figure 8d), both indicating that vertical momentum transfer is not inhibited across the
640 region.

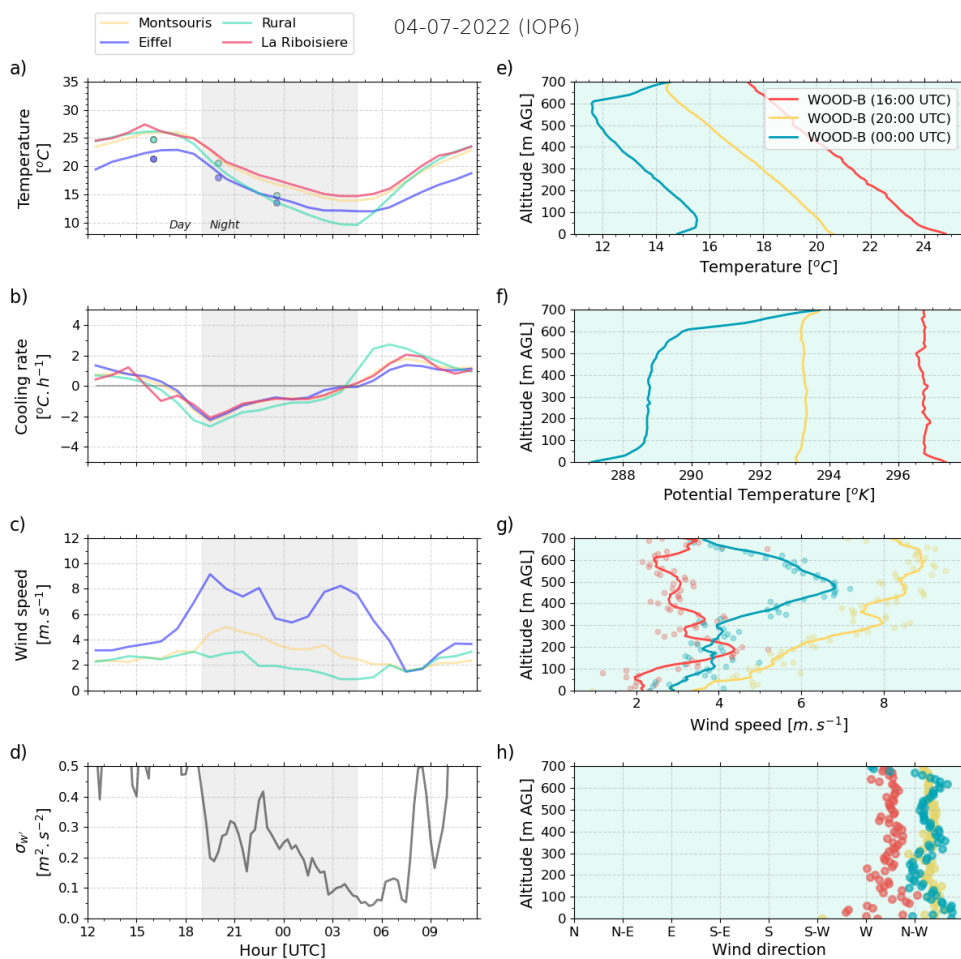
641

642 The windsond profiles carried out at the Bois de Boulogne large urban wood (WOOD-B in Fig.
643 1), detected a neutral UBL from 0 to 700 m AGL at 20 UTC. At 00 UTC, under continued brisk
644 turbulent mixing, a weak 1°C temperature inversion forms over the large green space while
645 the neutral UBL extends from 100m to 600 m AGL and is capped by a 5°C temperature
646 inversion.

647

648

649



650

651 Figure 8: same as Fig. 5 for July 04, 2022

652

653

654

655

656

657

658

659

660



661 5 - Characteristics and impacts of turbulence 662 regimes

663

664 To better understand the impact of wind, turbulence and static stability on differential cooling
665 between built-up areas, urban parks and rural settings, we analyse the characteristics of the
666 three turbulence regimes encountered during summer 2022. First, we study the diurnal
667 evolution of wind and turbulence in built-up settings, urban green spaces and rural
668 surroundings (Section 5.1) and then investigate the atmospheric static stability in the built-up
669 surfaces and green infrastructures (Section 5.2) for the three regimes. Finally, we analyse the
670 diurnal cycle of temperature and discuss the nocturnal cooling in built-up environments,
671 green infrastructures and rural settings for the three regimes (Section 5.3).

672 5.1 Wind and turbulent mixing characteristics of turbulence 673 regimes

674 First, we study how wind speed evolves at diurnal scales over the city (Montsouris urban
675 park), in the rural setting (Melun), and aloft (top of Eiffel Tower) for the turbulence regimes
676 identified in Section 3 (Fig. 9).

677

678 In the stagnant regime (highest UHI intensity and lowest vertical velocity variance), we find
679 that at sunset, when vertical mixing drops, the wind speed aloft increases while the near-
680 surface wind speed decreases both over the urban park and in the rural setting (Fig. 9a).
681 Vertical velocity variance reaches values below $0.05 \text{ m}^2 \text{ s}^{-2}$ shortly after sunset. Not only the
682 rural nocturnal boundary layer but also the UBL becomes stratified, thereby inhibiting vertical
683 transfer of momentum. The stable UBL becomes decoupled from the neutral layer above,
684 allowing near-surface wind speeds to decrease, on average below 2 m s^{-1} , through surface
685 drag, while wind speed aloft experiences reduced friction and hence increases.

686

687 In the intermediate regime (strong ΔUHI and moderate vertical velocity variance), we observe
688 that on average, the vertical velocity variance decreases later than in the stagnant regime and
689 it is 50 % stronger at sunset, reaching $0.15 \text{ m}^2 \text{ s}^{-2}$ on average during the night (Fig. 9b). The

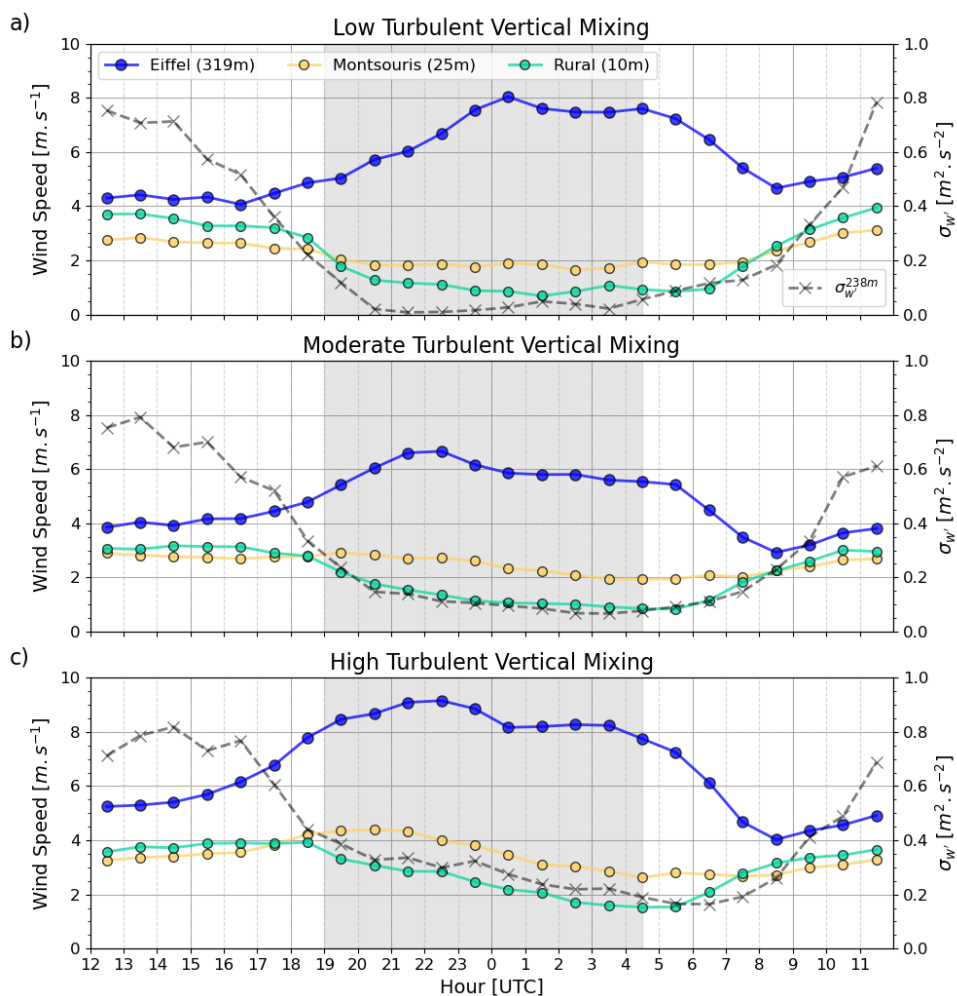


690 near-surface wind speed in the rural setting decreases at sunset similarly to the stagnant
691 regime, so we can hypothesise that the atmosphere becomes stable in the rural environment.
692 In the urban green spaces, the near-surface wind speed remains unchanged after sunset,
693 which is consistent with a continued vertical transfer of momentum. Still, the stable
694 stratification over the rural area tends to favour the formation of a low-level jet, a
695 phenomenon that occurs in Paris in 70% of the nights in summer 2022 (Cespedes et al. 2024),
696 so that the wind speed above the neutral UBL can double in magnitude between noon and
697 midnight.

698

699 In the turbulent regime (low UHI intensity and high vertical velocity variance) vertical velocity
700 variance in the UBL is on average above $0.3 \text{ m}^2 \text{ s}^{-2}$ at sunset (Fig. 9c). Near-surface wind speed
701 in the rural setting remains above 3 m s^{-1} on average, while central urban wind speeds
702 increase consistently across the UBL, i.e. both near the surface and at the top of the Eiffel
703 Tower.

704



705

706 Figure 9 : Average diurnal cycles over summer 2022 for each of the turbulence regimes
 707 (stagnant at the top, intermediary in the middle, and turbulent at the bottom): wind speed
 708 measured at Melun (rural site); Montsouris park (urban park); top of Eiffel Tower; and vertical
 709 velocity variance at 238 m AGL derived from Doppler Lidar measurements.

710 5.2 Atmospheric stability characteristics of turbulence regimes

711

712 In Section 4, we found evidence that the static stability above urban parks and urban woods
 713 can vary significantly depending on the turbulent vertical mixing in the UBL. To study this
 714 variability, we derive the potential temperature lapse rates for each windsound profile carried



715 out at 20 and 00 UTC above urban woods and parks, as well as radiosonde profiles launched
716 at the same time from the built-up area of Bercy (URBAN-B location on Fig. 1) along the Seine
717 river, and plot them against the vertical velocity variance estimated from the DWL
718 measurements at the same time (Fig. 10). The potential temperature lapse rate is derived for
719 two vertical intervals, 0-50 m AGL representing the height over which surface-based
720 inversions are typically observed (also called park/wood internal boundary layer), and 100-
721 200 m AGL representing the nocturnal UBL. Vertical velocity variances shown in Fig. 10 are
722 one-hour average values. The turbulence regime derived for each evening (19-02 UTC) is also
723 shown. Fig. 10b reveals that, when the vertical velocity variance drops below $0.05 \text{ m}^2 \text{ s}^{-2}$
724 (corresponding mostly to the stagnant regime) the near-surface potential temperature lapse
725 rate above urban parks (about 20 ha) ranges $4\text{-}6^\circ\text{C}/100 \text{ m}$ while those above the woods (about
726 900 ha) can reach $8\text{-}14^\circ\text{C}/100 \text{ m}$. In the lowest vertical velocity variance conditions (< 0.025
727 $\text{m}^2 \text{ s}^{-2}$), near-surface potential temperature lapse rates in built-up areas also become positive
728 ranging $1\text{-}3^\circ\text{C}/100 \text{ m}$. This confirms that stable stratification can occur in all settings, but the
729 strength of the stratification depends on the surface type.

730 For vertical velocity variances ranging $0.1\text{-}0.2 \text{ m}^2 \text{ s}^{-2}$, near-surface potential temperature lapse
731 rates above parks and woods range between $0\text{-}3^\circ\text{C}/100 \text{ m}$, decreasing to near adiabatic
732 conditions ($0^\circ\text{C}/100 \text{ m}$) as turbulent mixing increases. In built-up areas, we find that near-
733 surface potential temperature lapse rates become negative (near $-1^\circ\text{C}/100 \text{ m}$) as soon as the
734 vertical velocity variance exceeds $0.05 \text{ m}^2 \text{ s}^{-2}$, a signature of a typical unstable urban surface
735 layer.

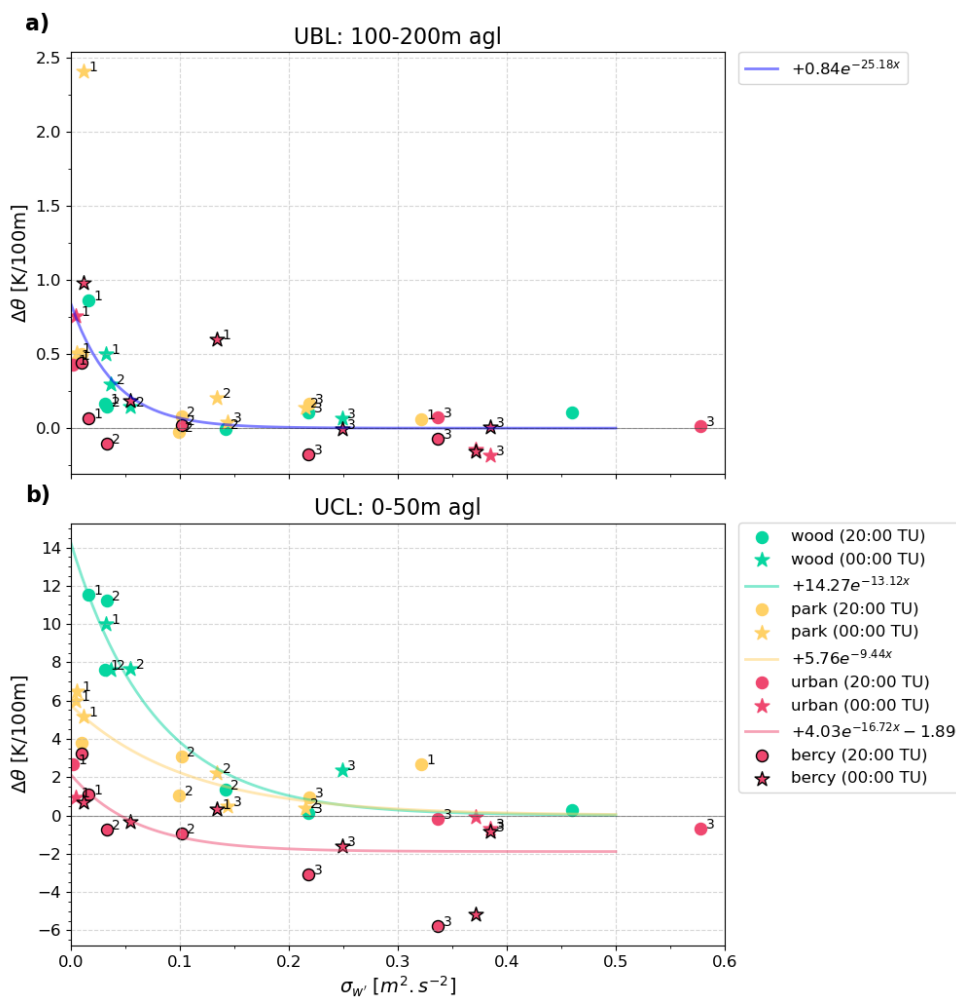
736 This analysis provides quantitative evidence that evening and night-time air temperature
737 conditions in the UCL become spatially heterogeneous when turbulent mixing in the UBL is
738 very weak. Only then it is possible for a strong temperature inversion to form over the urban
739 green space through the support of radiative flux divergence. The cool air remains in a local,
740 internal park/wood thermal boundary layer and does not mix with the relatively warm air in
741 the surrounding neighbourhoods. The significance and vertical extent of this cool air pool
742 increases with green space size, and it can be speculated that also green fraction and soil
743 moisture levels would enhance the effect.

744

745 The turbulent mixing in the UBL varies with the static stability of the UBL. As shown in Fig.
746 10a, when the potential temperature lapse rate at 100-200 m AGL increases to values near



747 +0.5°C/100m for all settings, including built-up areas, the vertical velocity variance decreases
 748 below 0.05 m² s⁻². No clear contrast in stability is found above the different surfaces,
 749 confirming that under the stagnant regime, the nighttime UBL is very shallow.
 750



751



752 Figure 10: Nighttime (20 and 00 UTC) potential temperature lapse rate above wood (green),
753 park (orange) and built-up areas (red) as a function of σ_w in the UBL (at 240 m AGL) for (a) a
754 layer between 100-200 m AGL and (b) a layer between 0-50 m AGL. Symbols indicate time
755 UTC. Urban labels with black borders correspond to data from radiosoundings launched from
756 the URBAN-B site and the others to data from windsonds (various sites). The number shows
757 the mean evening (19-02 UTC) turbulence regime for each case.

758

759 5.3 Impact of turbulence regimes on diurnal temperature 760 evolution

761

762 Ultimately, we want to determine how the turbulence regimes can impact the nocturnal
763 cooling provided by urban green infrastructures. Figure 11 shows the mean diurnal cycles of
764 temperature for stagnant, intermediary and turbulent regimes (a, b, and c, respectively). The
765 temperature diurnal cycles are normalised by subtracting the temperature measured at 16
766 UTC (peak daytime temperature). On average, daytime peak temperatures are highest for the
767 stagnant regime near 31°C, while they peak at about 27°C for the other two regimes. Figure
768 11 shows that after 16 UTC, the temperature at all sites decreases to reach a minimal value
769 the next morning at sunrise. In 12 hours, the temperatures drop between 8 and more than
770 14°C depending on the surface type and the turbulence regime. The stagnant regime reveals
771 the strongest contrasts between the settings (Fig. 11a). At 00 UTC, five hours after sunset, the
772 built-up neighbourhood cooled by 5.5°C, while the urban park cooled by 9.0°C and the rural
773 sites by almost 13.8°C. This confirms earlier findings (Table 2 and Section 5.2) that under low
774 turbulent vertical mixing, the radiative cooling of the surface in urban park and rural settings
775 combined with low turbulent vertical mixing provides an efficient cooling of the near-surface
776 atmosphere. In such conditions, urban parks can provide significantly cooler conditions than
777 the built-up neighbourhoods nearby.

778 In the intermediary regime, the evening cooling rate in the built-up environment is slightly
779 larger than for the stagnant regime (-6.2°C at 00 UTC, Fig. 11b). In the urban park, the
780 increased UBL turbulent vertical mixing reduces the strength of the near-surface radiative flux
781 divergence. The evening cooling in the urban park is not as strong (-7.5°C at 00 UTC) as in the



782 stagnant regime. In the rural setting, the evening cooling is also reduced in the intermediary
783 regime (-11.7°C at 00 UTC) compared to the stagnant regime, revealing that turbulence is also
784 likely stronger in the rural nocturnal boundary layer.

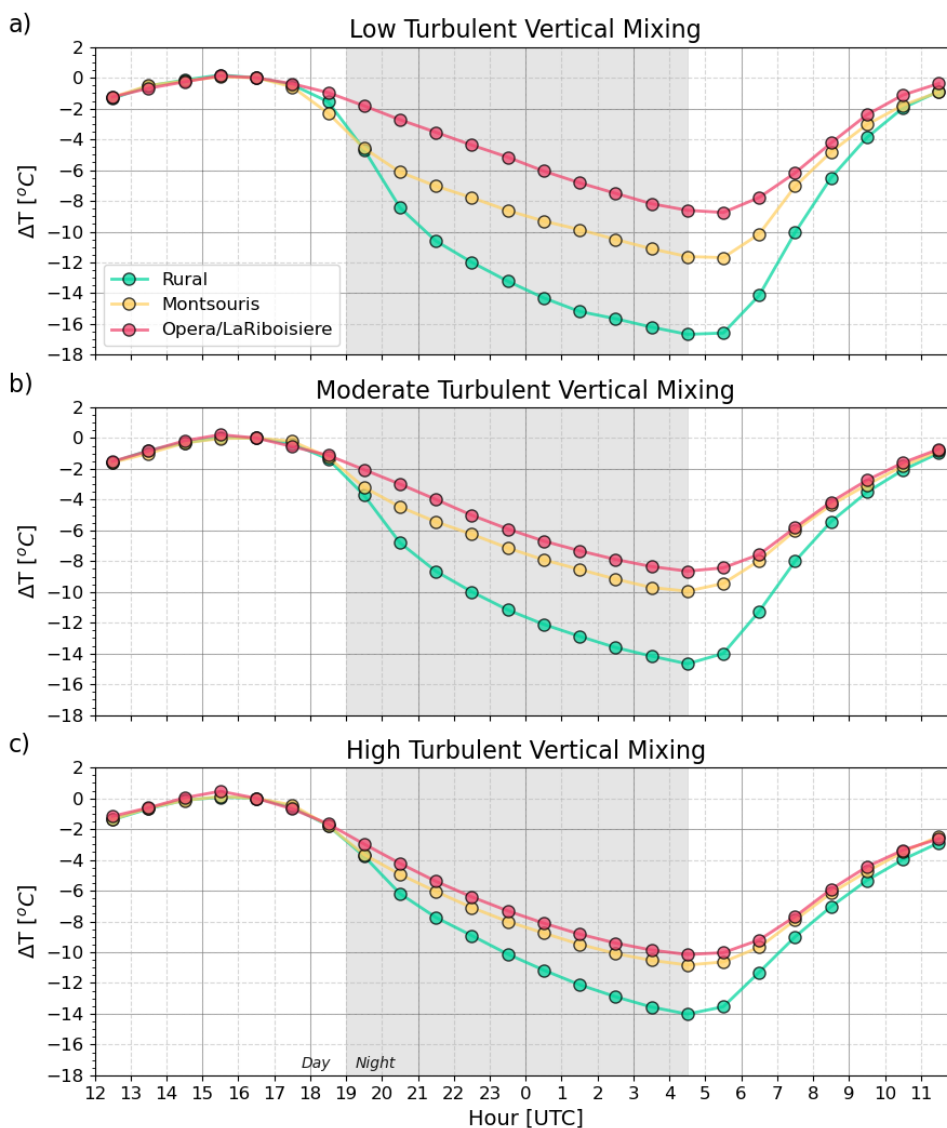
785 In the turbulent regime, with stronger turbulent vertical mixing and higher near-surface wind
786 speed than in the other regimes, the efficiency of the surface-driven cooling in the rural
787 setting is even more reduced, which limits the cooling compared to less turbulent conditions
788 (-10.6°C at 00 UTC, Fig. 11c). In the built-up environment, the air temperature drops by 7.6°C
789 between 16 and 00 UTC, i.e. 1.5-2°C more than in the other regimes. In this turbulent regime,
790 the city centre benefits from the cooling of the rural surroundings through advection – the
791 cooler air is mixed down into the UBL. In the urban park, two competing processes occur. The
792 radiative flux divergence is reduced by the strong mixing, but this again means cooler air
793 advected from rural surroundings is efficiently mixed down thereby contributing to a strong
794 cooling also in the urban park. Hence, we find that the temperature drops by 8.3°C on average
795 between 16 and 00 UTC, which is in between the stagnant and intermediary regime cooling.

796

797

798

799



800

801 Figure 11: diurnal cycle of temperature difference relative to the temperature at 16 UTC at
802 Melun (rural site), Montsouris park (urban park) and Opera/Lariboisiere (Built-up setting) for
803 stagnant, intermediary and turbulent regimes.

804

805



806 6) Conclusions

807 This study shows that the nocturnal cooling effect of urban parks depends on their
808 characteristics, such as their size, but also on UBL turbulent mixing and static stability regimes
809 that drive the relative importance of radiative and mixing transport cooling processes in the
810 UCL. We find that turbulent vertical mixing conditions measured by a Doppler Lidar at about
811 240 m AGL in the city centre is a very useful indicator to distinguish different evening cooling
812 regimes in the urban environment.

813

814 Highest green space nocturnal cooling intensity occurs under stable stratification in the UBL
815 (statically stable, low turbulent mixing: vertical velocity variance of less than $0.05 \text{ m}^2 \text{ s}^{-2}$) over
816 both rural settings and urban parks. This stagnant regime is associated with large-scale
817 subsidence and large-scale advection of warm air aloft. The potential temperature profiles
818 above the urban parks and woods become statically stable soon after sunset due to radiative
819 cooling of the surface and subsequent cooling of the air by radiative flux divergence, in the
820 absence of a significant turbulent heat flux. A few hours after sunset, the entire UBL becomes
821 on average statically stable (about 200-300 m deep) due to subsidence and advection of the
822 stable rural air above the urban environment. Even if the heat release from the urban surface
823 would in theory lead to an unstable/near neutral urban boundary layer at night, we observe
824 that the strong stabilisation from above limits it strongly in height, or even totally inhibits it.
825 At the top of the UBL, a low-level jet develops over the night with peak wind speed, but
826 mechanical turbulence is inhibited by the static stability of the UBL. The advected rural air
827 mass remains stable above the urban environment because of unusually low vertical mixing
828 conditions. This stagnant regime exhibits the strongest evening cooling in both rural settings
829 and urban parks, and the weakest cooling in the built-up environment, hence strong nocturnal
830 temperature contrasts occur in the city depending on the vegetation fraction. In this regime,
831 the cooling effect of green infrastructure will depend on their size and likely on the vegetation
832 fraction of these areas. In this stagnant regime, we find comparable nocturnal cooling rates
833 (peaking at -2°C/hr around sunset) and static stability in the UCL (lapse rate near $6^\circ\text{C}/100\text{m}$
834 at 00 UTC) above the Montsouris park (15 ha) and the Eiffel tower park (24 ha) that are
835 roughly of the same size.

836



837 A second regime is identified, characterised by moderate turbulent vertical mixing in the UBL
838 (for vertical velocity variance between 0.1 and 0.2 m² s⁻²). Under this intermediary regime, the
839 potential temperature profiles above the urban park become neutral after sunset. A small
840 temperature inversion (<0.5°C) can be found in the UCL. A few hours after sunset, the UBL
841 remains statically neutral up to 200-300 m due to positive turbulent heat flux at the surface
842 and at the top of the UBL which is characterised by a temperature inversion. Advection of
843 rural air brings a statically stable layer above the UBL. Under this intermediary regime, the
844 evening cooling in rural settings is about 2°C less than in the stagnant regime. Two hours after
845 sunset, the cooling in the urban park is also 2°C less than in the stagnant regime, while the
846 built-up environment is slightly cooler. There is probably vertical and also horizontal air mixing
847 (advection or local turbulence), which diminishes the cooling effect of small to medium-sized
848 parks (15-25ha) by mixing air from surrounding dense neighbourhoods. Hence in the
849 intermediary regime the intra-urban temperature contrasts between areas with varying
850 vegetation fractions are significantly reduced.

851

852 The third regime identified in this study results in the weakest nocturnal temperature
853 contrasts. Compared to the stagnant and intermediary regimes, the turbulent regime is
854 characterised by stronger advection and mesoscale circulation, wind shear and turbulent
855 vertical mixing. The UBL above the urban park becomes neutral after sunset, with a depth
856 that is significantly increased (>600 m) compared to the two other regimes. The UBL remains
857 neutral even several hours after sunset. In this regime, the evening cooling rates are nearly
858 identical in the built-up environment and in the urban parks. In the turbulent regime, high
859 turbulence and wind mix the air and homogenise temperatures at a larger scale (district-to-
860 city scale) than in the intermediary regime (neighbourhood scale), completely encompassing
861 and erasing the cooling effect of parks.

862

863 As statically stable low turbulent mixing conditions occur during the strongest heat waves due
864 to large-scale subsidence and advection of hot air, it is important to maintain spatially
865 distributed and accessible vegetated cool island spots in the city so that people can benefit
866 from cooler outdoor night-time conditions after being exposed to significant daytime heat
867 stress.

868



869 Data availability

870 All raw data are available from the AERIS data centre catalogue at <https://paname.aeris->

871 [data.fr/data-catalogue-2/](https://paname.aeris-data.fr/data-catalogue-2/).

872

873 Author contributions

874 MH, SK, AL, and VM planned the campaign; MH, SK, JFR, JCD and JC performed the

875 measurements; MH, JFR, SK and JC analysed the data; MH and SK wrote the manuscript draft;

876 JFR produced the figures; AL, VM and TN reviewed and edited the manuscript.

877

878 Competing interests

879 The authors declare that they have no conflict of interest.

880

881 Acknowledgements

882

883 The PANAME experimental program benefited from several supports, including the research

884 project H2C funded by the French national agency for research (ANR) with the reference ANR-

885 20-CE22-0013, the Research Demonstration Project for Paris Olympics 2024 funded by

886 Météo-France and the Weather Meteorological Organization, the Paris Region PhD program

887 2020, investments from DIM Q12, OBS4CLIM-PIA3, CNRS-INSU and the ACTRIS research

888 infrastructure, and data management (AERIS national data and services center). The authors

889 would like to thank all the volunteers and participants who contributed to the success of the

890 SOP 2022, in particular the teams and many volunteers who carried out the windsonde

891 releases in the parks in the evening and at night and the radiosoundings at Bercy. Thanks are

892 extended to Hugo Ricketts for training the IPSL team to operate windsonds, with the support

893 of the European COST action PROBE. Authors would like to express their thanks to the

894 QUALAIR-SU scientific team who enabled the Doppler Lidar deployment on the site at



895 Sorbonne Université.

896

897 References

898 Aram, F. E. Higuera García, E. Solgi, S. Mansournia. Urban green space cooling effect in cities.

899 Heliyon 5 (2019) e01339. doi: [10.1016/j.heliyon.2019.e01339](https://doi.org/10.1016/j.heliyon.2019.e01339)

900 Barradas, V.L. Air temperature and humidity and human comfort index of some city parks of
901 Mexico City. *Int J Biometeorol* 35, 24–28 (1991). <https://doi.org/10.1007/BF01040959>

902

903 Rupa Basu, Jonathan M. Samet, Relation between Elevated Ambient Temperature and
904 Mortality: A Review of the Epidemiologic Evidence, *Epidemiologic Reviews*, Volume 24, Issue
905 2, December 2002, Pages 190–202, <https://doi.org/10.1093/epirev/mxf007>

906

907 Barthelmie, R. J., Grisogono, B., & Pryor, S. C. (1996). Observations and simulations of diurnal
908 cycles of near-surface wind speeds over land and sea. *Journal of Geophysical Research:*
909 *Atmospheres*, 101(D16), 21327–21337. <https://doi.org/10.1029/96JD01520>

910

911 Dahech, S., Charfi, S., & Madelin, M. (2020). Représentativité des températures mesurées
912 dans la station météorologique Paris-Montsouris. *Climatologie*, 17, 5.
913 <https://doi.org/10.1051/climat/202017005>

914

915 Bowler D. E., Lisette Buyung-Ali, Teri M. Knight, Andrew S. Pullin, Urban greening to cool
916 towns and cities: A systematic review of the empirical evidence, *Landscape and Urban*
917 *Planning*, Volume 97, Issue 3, 2010, Pages 147–155, ISSN 0169-2046,
918 <https://doi.org/10.1016/j.landurbplan.2010.05.006>

919

920 Cai, X., Yang, J., Zhang, Y. *et al.* Cooling island effect in urban parks from the perspective of
921 internal park landscape. *Humanit Soc Sci Commun* 10, 674 (2023).
922 <https://doi.org/10.1057/s41599-023-02209-5>

923



- 924 Chang C. C., Ming-Huang Li, Shyh-Dean Chang, A preliminary study on the local cool-island
925 intensity of Taipei city parks, *Landscape and Urban Planning*, Volume 80, Issue 4, 2007, Pages
926 386-395, ISSN 0169-2046, <https://doi.org/10.1016/j.landurbplan.2006.09.005>
927
- 928 Céspedes, J., Kotthaus, S., Preissler, J., Toupoint, C., Thobois, L., Drouin, M.-A., Dupont, J.-C.,
929 Faucheux, A., and Haeffelin, M.: The Paris Low-Level Jet During PANAME 2022 and its Impact
930 on the Summertime Urban Heat Island, *EGUsphere* [preprint],
931 <https://doi.org/10.5194/egusphere-2024-520>, 2024.
932
- 933 Doick K. J., A. Peace, T. R. Hutchings, The role of one large greenspace in mitigating London's
934 nocturnal urban heat island, *Science of The Total Environment*, Volume 493, 2014, Pages 662-
935 671, ISSN 0048-9697, <https://doi.org/10.1016/j.scitotenv.2014.06.048>
936
- 937 Forceville G., A. Lemonsu, S. Gorla, M. Stempfelet, S. Host, J-M. Alessandrini, E. Cordeau, M.
938 Pascal, Spatial contrasts and temporal changes in fine-scale heat exposure and vulnerability
939 in the Paris region, *Science of The Total Environment*, Volume 906, 2024, 167476, ISSN 0048-
940 9697, <https://doi.org/10.1016/j.scitotenv.2023.167476>
941
- 942 Grimmond, C. S. B., and T. R. Oke, 2002: Turbulent Heat Fluxes in Urban Areas: Observations
943 and a Local-Scale Urban Meteorological Parameterization Scheme (LUMPS). *J. Appl. Meteor.*
944 *Climatol.*, 41, 792–810, [https://doi.org/10.1175/1520-0450\(2002\)041<0792:THFIUA>2.0.CO;2](https://doi.org/10.1175/1520-0450(2002)041<0792:THFIUA>2.0.CO;2).
945
946
- 947 Haeffelin M, Barthès L, Bock O, Boitel C, Bony S, Bouniol D, Chepfer H, Chiriaco M, Cuesta J,
948 Delanoë J, Drobinski P, Dufresne J-L, Flamant C, Grall M, Hodzic A, Hourdin F, Lapouge F,
949 Lemaître Y, Mathieu A, Morille Y, Naud C, Noël V, O'Hirok W, Pelon J, Pietras C, Protat A,
950 Romand B, Scialom G, Vautard R (2005) SIRTA, a ground-based atmospheric observatory for
951 cloud and aerosol research. *Ann Geophys* 23:253–275, <https://doi.org/10.5194/angeo-23-253-2005>.
952
953



954 Holmer, B., Thorsson, S., & Lindén, J. (2013). Evening evapotranspirative cooling in relation to
955 vegetation and urban geometry in the city of Ouagadougou, Burkina Faso. *International*
956 *Journal of Climatology*, 33(15), 3089-3105 , <https://doi.org/10.1002/joc.3561>.

957

958 Ibsen, P. C., Borowy, D., Dell, T., Greydanus, H., Gupta, N., Hondula, D. M., ... & Jenerette, G.
959 D. (2021). Greater aridity increases the magnitude of urban nighttime vegetation-derived air
960 cooling. *Environmental Research Letters*, 16(3), 034011, DOI 10.1088/1748-9326/abdf8a

961

962 Keatinge W R, Donaldson G C, Cordioli E, Martinelli M, Kunst A E, Mackenbach J P et al. Heat
963 related mortality in warm and cold regions of Europe: observational study *BMJ* 2000; 321 :670
964 doi:10.1136/bmj.321.7262.670

965

966 Laj, P., Lund Myhre, C., Riffault, V., Amiridis, V., Fuchs, H., Eleftheriadis, K., ... & Vana, M.
967 (2024). Aerosol, Clouds and Trace Gases Research Infrastructure–ACTRIS, the European
968 research infrastructure supporting atmospheric science. *Bulletin of the American*
969 *Meteorological Society*. <https://doi.org/10.1175/BAMS-D-23-0064.1>

970

971 Lemonsu, A., Belair, S. & Mailhot, J. The New Canadian Urban Modelling System: Evaluation
972 for Two Cases from the Joint Urban 2003 Oklahoma City Experiment. *Boundary-Layer*
973 *Meteorol* 133, 47–70 (2009). <https://doi.org/10.1007/s10546-009-9414-2>

974

975 Lemonsu, A., V. Vigié, M. Daniel, V. Masson, Vulnerability to heat waves: Impact of urban
976 expansion scenarios on urban heat island and heat stress in Paris (France), *Urban Climate*,
977 Volume 14, Part 4, 2015, Pages 586-605, ISSN 2212-0955,
978 <https://doi.org/10.1016/j.uclim.2015.10.007>.

979

980 Lemonsu, A., J.M. Alessandrini, J. Capo, M. Claeys, E. Cordeau, C. de Munck, S. Dahech, J.C.
981 Dupont, F. Dugay, V. Dupuis, G. Forceville, S. Garrigou, O. Garrouste, M. Goret, S. Gorla, M.
982 Haeffelin, S. Host, C. Joly, P. Keravec, S. Kotthaus, N. Laruelle, M. Madelin, V. Masson, C.
983 Mauclair, T. Nagel, M. Pascal, J.F. Ribaud, G. Roberts, A. Rosso, A. Roy, M. Sabre, O. Sanchez,
984 M. Stempfelet, W. Wei, R. Wilson, J. Wurtz, The heat and health in cities (H2C) project to



985 support the prevention of extreme heat in cities, *Climate Services*, 2024, 100472, ISSN 2405-
986 8807, <https://doi.org/10.1016/j.cliser.2024.100472>
987
988 Lemonsu A., Barrau S., Capo J., Céspedes J., Dahech S., de Munck C., Dumas G., Dupont J.-C.,
989 Dupuis V., Etienne J.-C., Garrouste O., Goret M., Haeffelin M., Keravec P., Kotthaus S., Madelin
990 M., Martinet P., Masson V., Nagel T., Price J., Ribaud J.-F., Rivollet M., Roberts G., Roy A.,
991 Unger, V., Wilson R., Wallois S., Wurtz J., Multi-scale study of urban-atmosphere interactions
992 in the Paris region (France) in the framework of the PANAME experiment, *Bull. Am. Met. Soc.*
993 Submitted 2024.
994
995 Lin, Y., C. Wang, J. Yan, J. Li, and S. He, 2022: Observation and Simulation of Low-Level Jet
996 Impacts on 3D Urban Heat Islands in Beijing: A Case Study. *J. Atmos. Sci.*, 79, 2059–2073,
997 <https://doi.org/10.1175/JAS-D-21-0245.1>.
998
999 Martilli, A., 2002: Numerical Study of Urban Impact on Boundary Layer Structure: Sensitivity
1000 to Wind Speed, Urban Morphology, and Rural Soil Moisture. *J. Appl. Meteor. Climatol.*, 41,
1001 1247–1266, [https://doi.org/10.1175/1520-0450\(2002\)041<1247:NSOUIO>2.0.CO;2](https://doi.org/10.1175/1520-0450(2002)041<1247:NSOUIO>2.0.CO;2).
1002
1003 Morris, C. J. G., I. Simmonds, and N. Plummer, 2001: Quantification of the Influences of Wind
1004 and Cloud on the Nocturnal Urban Heat Island of a Large City. *J. Appl. Meteor. Climatol.*, 40,
1005 169–182, [https://doi.org/10.1175/1520-0450\(2001\)040<0169:QOTIOW>2.0.CO;2](https://doi.org/10.1175/1520-0450(2001)040<0169:QOTIOW>2.0.CO;2).
1006
1007 Murage, Peninah; Hajat, Shakoore; Kovats, R. Sari. Effect of night-time temperatures on cause
1008 and age-specific mortality in London. *Environmental Epidemiology* 1(2):p e005, December
1009 2017. | DOI: 10.1097/EE9.0000000000000005
1010
1011 Oke, T. R. (1976). The distinction between canopy and boundary-layer urban heat islands.
1012 *Atmosphere*, 14(4), 268–277. <https://doi.org/10.1080/00046973.1976.9648422>
1013
1014 Oke, T.R. (1982), The energetic basis of the urban heat island. *Q.J.R. Meteorol. Soc.*, 108: 1-
1015 24. <https://doi.org/10.1002/qj.49710845502>



1016

1017 Oke, T. Towards better scientific communication in urban climate. *Theor. Appl. Climatol.* 84,
1018 179–190 (2006). <https://doi.org/10.1007/s00704-005-0153-0>

1019

1020 Oke, T. R., Mills, G., Christen, A., & Voogt, J. A. (2017). *Urban climates*. Cambridge University
1021 Press.

1022

1023 Pirard P, Vandentorren S, Pascal M, Laaidi K, Le Tertre A, Cassadou S, Ledrans M. Summary of
1024 the mortality impact assessment of the 2003 heat wave in France. *Euro Surveill.*
1025 2005;10(7):pii=554. <https://doi.org/10.2807/esm.10.07.00554-en>

1026

1027 von Rohden, C., Sommer, M., Naebert, T., Motuz, V., & Dirksen, R. J. (2022). Laboratory
1028 characterisation of the radiation temperature error of radiosondes and its application to the
1029 GRUAN data processing for the Vaisala RS41. *Atmospheric Measurement Techniques*, 15(2),
1030 383-405.

1031

1032 Royé, Dominic; Sera, Francesco; Tobías, Aurelio; Lowe, Rachel; Gasparrini, Antonio; Pascal,
1033 Mathilde; de'Donato, Francesca; Nunes, Baltazar; Teixeira, Joao Paulo. Effects of Hot Nights
1034 on Mortality in Southern Europe. *Epidemiology* 32(4):p 487-498, July 2021. | DOI:
1035 10.1097/EDE.0000000000001359

1036

1037 Shashua-Bar, L., M.E. Hoffman, Vegetation as a climatic component in the design of an urban
1038 street: An empirical model for predicting the cooling effect of urban green areas with trees,
1039 *Energy and Buildings*, Volume 31, Issue 3, 2000, Pages 221-235, ISSN 0378-7788,
1040 [https://doi.org/10.1016/S0378-7788\(99\)00018-3](https://doi.org/10.1016/S0378-7788(99)00018-3)

1041

1042 Steeneveld, G. J., B. J. H. van de Wiel, and A. A. M. Holtslag, 2006: Modeling the Evolution of
1043 the Atmospheric Boundary Layer Coupled to the Land Surface for Three Contrasting Nights in
1044 CASES-99. *J. Atmos. Sci.*, 63, 920–935, <https://doi.org/10.1175/JAS3654.1>.

1045

1046 Steeneveld, G. J., M. J. J. Wokke, C. D. Groot Zwaaftink, S. Pijlman, B. G. Heusinkveld, A. F. G.
1047 Jacobs, and A. A. M. Holtslag (2010), Observations of the radiation divergence in the surface



1048 layer and its implication for its parameterization in numerical weather prediction models, *J.*
1049 *Geophys. Res.*, 115, D06107, doi:[10.1029/2009JD013074](https://doi.org/10.1029/2009JD013074).
1050
1051 Taha, H., Akbari, H. & Rosenfeld, A. Heat island and oasis effects of vegetative canopies:
1052 Micro-meteorological field-measurements. *Theor Appl Climatol* 44, 123–138 (1991).
1053 <https://doi.org/10.1007/BF00867999>
1054
1055 Tsiringakis, A., Theeuwes, N.E., Barlow, J.F. *et al.* Interactions Between the Nocturnal Low-
1056 Level Jets and the Urban Boundary Layer: A Case Study over London. *Boundary-Layer*
1057 *Meteorol* **183**, 249–272 (2022). <https://doi.org/10.1007/s10546-021-00681-7>
1058
1059 Zhu, W.; Sun, J.; Yang, C.; Liu, M.; Xu, X.; Ji, C. How to Measure the Urban Park Cooling Island?
1060 A Perspective of Absolute and Relative Indicators Using Remote Sensing and Buffer Analysis.
1061 *Remote Sens.* 2021, *13*, 3154. <https://doi.org/10.3390/rs13163154>
1062
1063
1064
1065
1066

